3D adaptive optics in a light sheet microscope

Cyril Bourgenot, Christopher D. Saunter, Jonathan M. Taylor, John M. Girkin, and Gordon D. Love[*]

Department of Physics & Biophysical Sciences Institute, Durham University, Durham DH1 3LE, UK

[*] *g.d.love@durham.ac.uk*

Abstract: We report on a single plane illumination microscope (SPIM) incorporating adaptive optics in the imaging arm. We show how aberrations can occur from the sample mounting tube and quantify the aberrations both experimentally and computationally. A wavefront sensorless approach was taken to imaging a green fluorescent protein (GFP) labelled transgenic zebrafish. We show improvements in image quality whilst recording a 3D "z–stack" and show how the aberrations come from varying depths in the fish.

OCIS codes: (110.1080) Active or adaptive optics; (110.1085) Adaptive imaging; (110.0180) Microscopy.

References and links

1. J. M. Girkin, S. Poland, and A. J. Wright, "Adaptive optics for deeper imaging of biological samples," Curr. Opin. Biotechnol. **20**, 106–110 (2009).
2. M. J. Booth, "Adaptive optics in microscopy," Philos. Trans. R. Soc. London, Ser. A. **365**, 2829–2843 (2007).
3. M. Schwertner, M. J. Booth, M. A. A. Neil, and T. Wilson, "A Measurement of specimen- induced aberrations of biological samples using phase stepping interferometry," J. Microsc. **213**, 11–19 (2004).
4. M. Booth, M. Neil, and T. Wilson, "Aberration correction for confocal imaging in refractive-index- mismatched media," J. Microsc. **192**, 90–98 (1998).
5. D. Debarre, M. J. Booth, and T. Wilson, "Image based adaptive optics through optimisation of low spatial frequencies," Opt. Express **15**, 8176–8190 (2007).
6. M. J. Booth, M. A. A. Neil, R. Juskaitis, and T. Wilson, "Adaptive aberration correction in a confocal microscope," Proc. Natl. Acad. Sci. U.S.A. **99**, 5788–5792 (2002).
7. X. Tao, B. Fernandez, O. Azucena, M. Fu, D. Garcia, Y. Zuo, D. C. Chen, and J. Kubby, "Adaptive optics confocal microscopy using direct wavefront sensing," Opt. Lett. **36**, 1062–1064 (2011).
8. L. Sherman, J. Y. Ye, O. Albert, and T. B. Norris, "Adaptive correction of depth-induced aberrations in multiphoton scanning microscopy using a deformable mirror," J. Microsc. **206**, 65–71 (2002).
9. J. W. Cha and P. T. So, "A Shack-Hartmann wavefront sensor based adaptive optics System for multiphoton microscopy," in Biomedical Optics, OSA Technical Digest (CD) (Optical Society of America, 2008).
10. N. Olivier, D. Debarre, and E. Beaurepaire, "Dynamic aberration correction for multiharmonic microscopy," Opt. Lett. **34**, 3145–3147 (2009).
11. A. J. Wright, S. P. Poland, J. M. Girkin, C. W. Freudiger, C. L. Evans, and X. S. Xie, "Adaptive optics for enhanced signal in CARS microscopy," Opt. Express **15**, 18209–18219 (2007).
12. J. Huisken, J. Swoger, F. Del Bene, J. Wittbrodt, and E. H. K. Stelzer, "Optical sectioning deep inside live embryos by selective plane illumination microscopy," Science **305**, 1007–1009 (2004).
13. K. Greger, J. Swoger, and E. H. K. Stelzer, "Basic building units and properties of a fluorescence single plane illumination microscope," Rev. Sci. Instrum. **78**, 023705 (2007).
14. J. Huisken and D. Y. R. Stainier, "Selective plane illumination microscopy techniques in developmental biology," Development **136**, 1963–1975 (2009).
15. L. I. Zon, "Zebrafish: a new model for human disease," Genome Res. **9**, 99–100 (1999)
16. J. Bakkers, "Zebrafish as a model to study cardiac development and human cardiac disease," Cardiovasc. Res. **91**, 183–184 (2011).

#164711 - $15.00 USD Received 14 Mar 2012; revised 14 May 2012; accepted 15 May 2012; published 29 May 2012

17. A. J. Hill, H. Teraoka, W. Heideman, and R. E. Peterson, “Zebrafish as a model vertebrate for investigating chemical toxicity,” Toxicol. Sci. **86**, 6–19 (2005).
18. J. M. Taylor, C. D. Saunter, G. D. Love, J. M. Girkin, D. J. Henderson, and B. Chaudhry, “Real-time optical gating for three-dimensional beating heart imaging,” J. Biomed. Opt. **16**, 116021 (2011).
19. P. J. Verveer, J. Swoger, F. Pampaloni, K. Greger, M. Marcello, and E. H. Stelzer, “High-resolution three-dimensional imaging of large specimens with light sheet-based microscopy,” Nat. Methods **4**, 311–313 (2007).
20. J. Mertz, “Optical sectioning microscopy with planar or structured illumination,” Nat. Methods **8**, 811–819 (2011).
21. M. J. Booth, “Wave front sensor-less adaptive optics: a model-based approach using sphere packings,” Opt. Express **14**, 1339–1352 (2006).
22. A. Facomprez, E. Beaurepaire, and D. Debarre, “Accuracy of correction in modal sensorless adaptive optics,” Opt. Express **20**, 2598–2612 (2012).
23. K. N. Walker and R. K. Tyson, “Wavefront correction using a Fourier-based image sharpness metric,” Proc. SPIE. **7468**, 74680O (2009).
24. A. M. Petzold, V. M. Bedell, N. J. Boczek, J. J. Essner, D. Balciunas, K. J. Clark, and S. C. Ekker, “SCORE imaging: specimen in a corrected optical rotational enclosure,” Zebrafish **7**, 149–154 (2010).

---

1. Introduction

The use of adaptive optics (AO) in microscopy is a relatively new application of this technology that aims to increase imaging quality by reducing aberrations caused by the microscope optics, the mounting optics (usually a coverslip) and by the specimen itself [1–4]. AO has been used with a range of modalities, including wide field [5], confocal [6,7], multi-photon [8,9], multi-harmonic [10] and CARS (coherent anti-Stokes Raman scattering) microscopy [11]. In this paper we describe the use of AO in a selective plane illumination microscope (SPIM), also known as a light-sheet microscope [12,13]. From the perspective of AO, light sheet microscopy is interesting because the illumination and imaging paths are decoupled and AO can potentially be useful on both paths. In this paper we demonstrate a number of results. First we show AO applied to SPIM and show significant improvement in imaging quality of a 3D z–stack of a zebrafish embryo using a wavefront sensorless AO system on the imaging path. We show, both experimentally and computationally, that AO on the imaging path can be used to correct for beam displacement on both the illumination and imaging paths, as well as focus and higher order aberrations on the imaging path. Finally we quantify the aberrations as a function of depth in the sample.

SPIM is an attractive imaging modality due to its ability to deliver high-speed, optically sectioned images from within *in vivo* samples with reduced photo-damage. The sectioning is obtained by the use of a light sheet that selectively excites a slice of the sample at the focal plane of a microscope objective placed perpendicular to the illumination sheet, thus enabling an entire optical section to be recorded in a single camera exposure. The out of focus part of the sample is not illuminated and one can build up a z-stack by only scanning in one (z) dimension. Phototoxity and bleaching are reduced because the use of a light sheet means that parts of the sample which are not being imaged at a particular instant are not illuminated.

Zebrafish are interesting biologically because they can be used as a model for human disease [15] and the development of organs such as the heart [16], as well as drug testing [17]. Our interest is in the imaging of the heart, which is further complicated by the fact that it is moving. We previously demonstrated 3D reconstruction of a living, beating heart using SPIM, using real-time optical gating to record images at a consistent phase in the heart cycle [18]. To the best of our knowledge, there have been no published results on SPIM and AO, although alternative techniques such as post-processing deconvolution [19] or structured illumination [20] have been implemented to improve the contrast and resolution.

In section 2 we describe the experimental details and summarize the wavefront sensorless AO system. In section 3 we describe how aberrations can occur in a SPIM and show results taken with fluorescent beads in order to quantify and calibrate the system. In section 4 we describe

#164711 - $15.00 USD Received 14 Mar 2012; revised 14 May 2012; accepted 15 May 2012; published 29 May 2012

the results of wavefront correction wavefront correction with zebrafish samples

2. Experimental details

The AO-corrected SPIM is shown in Fig. 1. A water filled chamber encloses the excitation and emission objectives as well as the sample, which, for the first experiments, is held in a borosilicate tube (inner diameter: 1 mm, outer diameter: 1.5 mm and refractive index: 1.47). The excitation source is a 15 mW, 488 nm fiber coupled solid state laser which can deliver approx 8 mW to the sample, with a power density of approx 3 $\mu\text{W}\mu\text{m}^{-2}$ for the duration of the camera exposure in a layer. The beam is collimated and expanded (not shown here) before passing through a cylindrical lens L1 ($f = 50$ mm, $\Phi = 25.4$ mm) with the light sheet being formed in the image plane of a Nikon CFI Plan Fluor $10\times$ 0.3NA objective (m1). The fluorescence is subsequently collected through a Nikon CFI75 LWD $16\times$ 0.80NA objective (m2). The resulting fluorescent light is then directed onto an Imagine Optic Mirao 52-e deformable mirror (DM) (15 mm aperture, 52 magnetic actuators) with the help of a $4f$ relay composed of two achromatic doublets L2 ($f = 250$ mm, Φ25.4 mm) and L3 ($f = 200$ mm, Φ25.4 mm). An image is then formed on the science camera (QImaging retiga 1300) using L4 ($f = 250$ mm, Φ25.4 mm). F1 is a filter to select the fluorescent light. A 633 nm HeNe laser was used (via beamsplitter S1) to measure and calibrate the DM shape so the mirror is taught to generate specific Zernike modes via the use of interaction matrices. Once the mode calibration is complete, the HeNe laser was switched off and the wavefront sensor is no longer used. The wavefront amplitude is indirectly measured using wavefront sensorless AO, as described below. The calibration laser light covers 12.5 mm of the 15 mm useful diameter of the DM, which leads, at the microscope objective imaging plane, to an effective 0.68 NA. The laser is separated from the fluorescence beam by a dichroic D1, and sent onto a Shack-Hartmann wavefront sensor (WFS) ($f = 5$ mm, 40 x 32 sub-aperture, pitch 150 μm,) via a $4f$ relay composed of L5 ($f = 400$ mm, Φ25.4 mm) and L6 ($f = 75$ mm, Φ25.4 mm). F2 is a 633 nm interference filter to select only the HeNe laser.

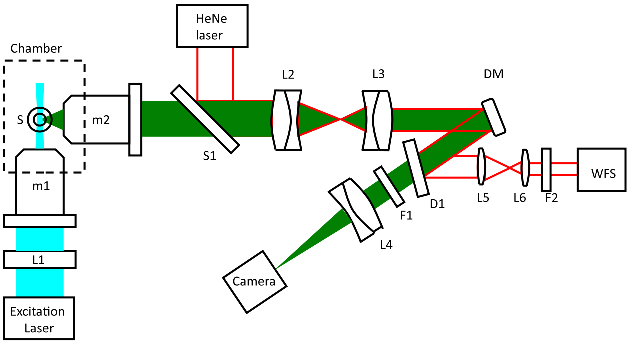

Fig. 1. Optical Configuration showing the SPIM and the AO. The illumination light is shown in blue - to the left, and the imaging light is shown in green, to the right. The symbols are explained in detail in the text.

Wavefront sensorless AO has been explained in detail in [21] and [22]. We used the "*PN*" algorithm (*P* is the number of images taken per mode and *N* is the number of modes), which consists of determining the proportion of each mode contributing to the aberration, by sequentially generating each mode on the DM with *P* varying amplitudes. The subsequent image quality, determined by an image quality metric, is recorded at the same time. From these data, the optimum amplitude is calculated for each mode. The use of a model, which describes the variation of the metric value with the aberration amplitude, can speed up the determination of the maximum as only a few points per mode are needed. We used a Lorentzian fit (which we found gave the best fit for larger amplitudes) and limited our analysis to low order Zernike modes (12 modes excluding piston, tip/tilt).

3. Sources of error in a SPIM and calibration

In [4], the wavefront distortion created by a refractive index mismatch at a planar interface between two media of different refractive indices was modeled analytically. This planar geometry, with no azimuthal variations, leads to symmetric aberrations varying with depth and aperture, and is well suited to conventional microscopy where the sample is placed between a slide and a coverslip. The situation is different in SPIM, and is shown schematically in Fig. 2. Both the illumination and imaging rays can be bent giving rise to displacement errors. In addition the beams are also affected by astigmatism (not shown in the figure). We produced a ray–tracing Zemax model of the system with the results shown in Fig. 3. The first contribution (dashed blue line) comes from the distortion of the light sheet due to the cylinder curved surface resulting in an axial shift along the emission path. As a consequence of this, when moving the sample (and therefore tube) by z, the light sheet was consequently moved by $z+\Delta z_1$, where Δz_1 is shown in Fig. 2. This effect is maximized at the edge of the tube, where the light sheet beam travels through highly inclined surfaces. The second effect (red dotted line) is a shift in the imaging rays due to the refraction in the glass tube. The resulting defocus term is the combination of both effects (green curve). They are combined by taking the difference - but then a constant offset is removed to force the combination to be zero at zero depth (since in practice that is the position where the system is manually focussed). We assumed a perfect aberration free objective lens (since we did not want to complicate the results with a separate issue). The results in Fig. 3 show that the model and the experimental results are close implying that the objective aberrations are small (as one would expect from a high quality objective).

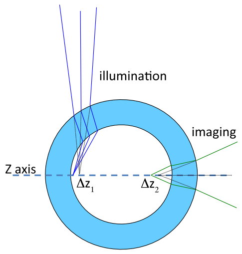

Fig. 2. Tube geometry used to hold the zebrafish. The light–blue ring shows the cross section of the pipette. The blue rays from the top show the illumination beam (only focussed in the direction shown - it is a sheet in the orthogonal direction), and the green rays on the right show the illumination rays. Normally the foci of each set of rays coincide but we have drawn them separately here for clarity. Both the illumination beam and the imaging beam foci can be significantly deviated, as shown (the undeviated rays are shown for comparison in black) and both can give rise to focus errors. The deviations are given by Δz_1 and Δz_2 respectively, and are shown numerically in Fig. 3. Light in the imaging arm is also significantly affected by astigmatism (not shown). The z–axis is shown, which is the scanning axis.

The parameters of the simulation are as follows: imaging arm NA is 0.68, tube thickness 0.25 mm, inner radius 0.50 mm, tube refractive index 1.47, and water index 1.33 at a wavelength of

0.55 μm close to the emission wavelength of the GFP used in our transgenic sample. There also was a small misalignment in our experiment between the focus of the imaging beam and the center of the tube, and this is accounted for in the simulation. We compared these simulation results with experiment by using a specimen with minimal aberrations (apart from the pipette) formed using 2 μm fluorescent beads embedded in 0.5% agarose held in a borosilicate glass pipette.

The sample was scanned in depth at 20 μm intervals, from the front to the back of the pipette and the images were corrected using the wavefront sensorless algorithm and the resulted wavefronts were calculated. Typical "before" and "after" images are shown in Figs. 4(a) and 4(b). The "before" image was recorded with the DM flat, confirmed using the Shack-Hartmann wavefront sensor and HeNe combination. The one-dimensionally elongated spot reveals that the main aberration is astigmatism, created by the cylindrical geometry. The variation in the normalized metric value (Eq. (1)) during the full optimization process is shown in Fig. 4(c). In principle we could have obtained the same data using the wavefront sensor. In practice the wavefront sensorless approach was easier because otherwise, for the Shack Hartmann, we would have had to isolate light from the beads from other light from the sample.

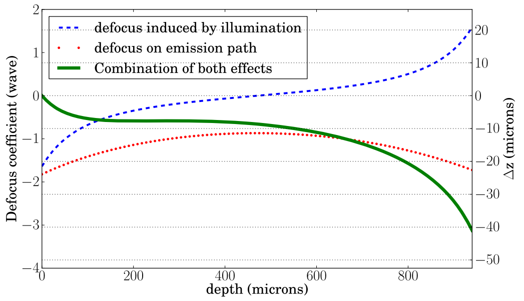

Fig. 3. Results of ray tracing in a mounting pipette showing how both the illumination beam (blue dashed line) and the imaging beam (red dotted beam) are deviated by the pipette (see Fig. 2) which gives rise to a focus error. The left hand ordinate shows the defocus measured in RMS waves and the right hand ordinate shows the same defocus expressed in terms of spot displacement, Δz (shown separately as Δz_1 and Δz_2 in Fig. 2). The green solid line is the combination (difference) of the two curves and is the net observed defocus - which has an additional constant offset removed so that the green (solid) line goes through the origin (since that is the point at which the microscope is manually focussed). Astigmatism was also simulated (and is shown in Fig. 4).

Four areas have been delimited in Fig. 4(c) by vertical dashed lines, each corresponding to a single optimization run performed on twelve Zernike modes (for j from 4 to 15, where j is the mode number). For each mode, P images were taken, and for each image a specific mode amplitude was produced as follows. In zone 1, $P = 3$ images per mode were recorded, with Zernike amplitudes varying from -2.5 to 2.5 waves RMS in order to make a coarse estimate of the aberrations. In zone 2 again $P = 3$ but with a reduced amplitude range (from -0.5 to 0.5 waves RMS) with the starting shape of the mirror being determined by the result calculated from zone 1. Zone 3 is a re-run of zone 2 - but using the starting values from zone 2. Then a final run was performed (zone 4) with $P = 7$ points per mode and the amplitude varying from -0.25 to +0.25 wave RMS.

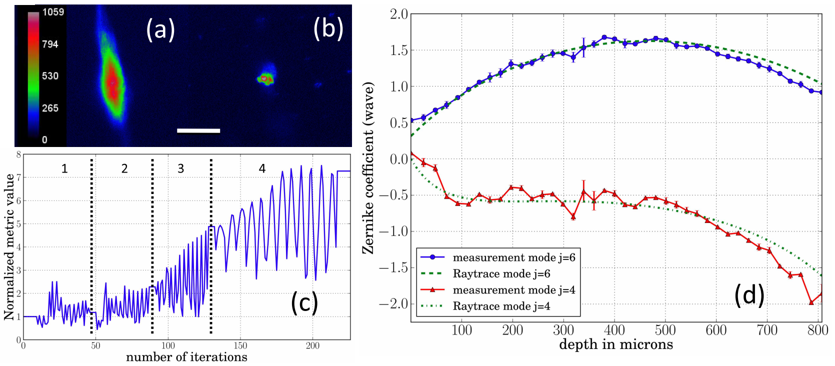

Fig. 4. Results of calibrating the system with beads. (a) image of the bead imaged through a borosilicate glass pipette when the DM is flat. (b) Image of the bead after optimization. The white scale bar represents 20 μm. (c) Variation of the metric during the 4 optimization runs (different zones are described in the text). (d) Measured and simulated focus and astigmatism variation with depth (Zernike modes j= 4 and 6) at a wavelength of 550 nm.

In zone 1, 2 and 3 the RMS contrast of the image was used as the metric, given by,

$$metric = \sqrt{\frac{1}{N_\mathrm{p}}\sum_{N_\mathrm{p}}\left(I(x,y)-\langle I\rangle\right)^2} \tag{1}$$

where $I(x,y)$ is the intensity for pixel (x,y), N_p is the number of pixels in the region of interest (ROI), $< I >$ represents the average intensity value over the ROI, and the sum is over all the pixels in the ROI. We found that when a large level of aberration is present in the image this metric provides excellent and reliable convergence. In zone 4 we used a metric maximizing the high spatial frequency [23], given by,

$$metric = \frac{\sum_{N_\mathrm{p}}|\mathscr{F}[I(x,y)]|_\mathrm{masked}}{\sum_{N_\mathrm{p}}|\mathscr{F}[I(x,y)]|_\mathrm{unmasked}}. \tag{2}$$

Here $\mathscr{F}[I(x,y)]$ describes the power spectral density (PSD) in the image (where $\mathscr{F}$ denotes the Fourier transform). The masked PSD is obtained by setting the values contained in a 5×5 pixel square mask positioned at the center of the 2D PSD to zero. The equivalent cut-off frequency is 9.3 μm^{-1}. With a low level of aberration in the image, we found that this metric was more appropriate. Figure 4(d) compares the simulated (green plots) and measured astigmatism (mode j = 6) amplitude, in blue, and focus (mode j = 4) amplitude, in red, with depth. The error bars were calculated during the final run (zone 4), and are defined by the Lorentzian fit error. They correspond to the difference between the measured amplitude giving the highest metric and the amplitude calculated with the fit. For both astigmatism and focus, there is a good fit between the measurement and the simulation. As expected with the glass pipette the astigmatism is the main aberration, reaching a maximum (1.6 waves RMS) at the centre of the cylinder. The simulation of the defocus variation with depth takes into account the two effects as described earlier. We have also produced an extended model showing the effects of the tube on the aberrations as we vary the tube parameters (thickness, refractive index, and N.A.). The complete results are beyond the scope of this paper and will be presented elsewhere.

4. Results for a zebrafish in a glass pipette and plastic tube

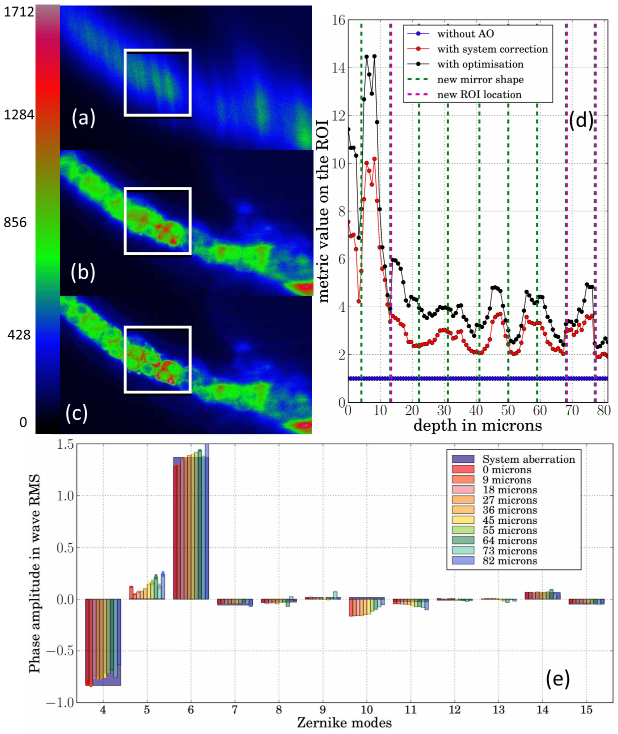

Fig. 5. AO in SPIM with a zebrafish in a glass borosilicate pipette. (a,b,c) are images taken for a flat mirror shape, a mirror shape optimized for the system aberrations, and for a mirror shape optimized directly on the fish. The white square corresponds to the ROI on which the optimization is performed and is 24 microns wide. (d) shows the metric normalized to the uncorrected values during the z-stack, as a function of imaging depth, when the mirror is flat (blue), and optimized (black). The green vertical lines correspond to where the mirror has been optimized. The purple vertical line shows when the ROI has been moved. (e) shows the Zernike mode amplitude at different depth. Mode 4 and mode 6 are focus and astigmatism, respectively. Two s are provided which show “before” and “after” full–AO examples. The first (Media 1) shows a z–scan through the dorsal fin and the second (Media 2) shows blood vessels in the fish.

An *ex-vivo* GFP transgenic Zebrafish was placed in water in the glass tube. A z-stack of images of the pectoral fin was recorded at ten axial positions, uniformly spaced over a depth of 82 μm. This part of the specimen has brightly labeled features with fine structure, and has the advantage of being placed on the side of the fish, and so could be placed to minimize illumination aberrations. For each of the ten depths an optimization was performed and the mirror shape recorded after using the final Fourier metric optimization described in Eq. (2) above. As the features change along the z–stack, the ROI was moved such that it remained

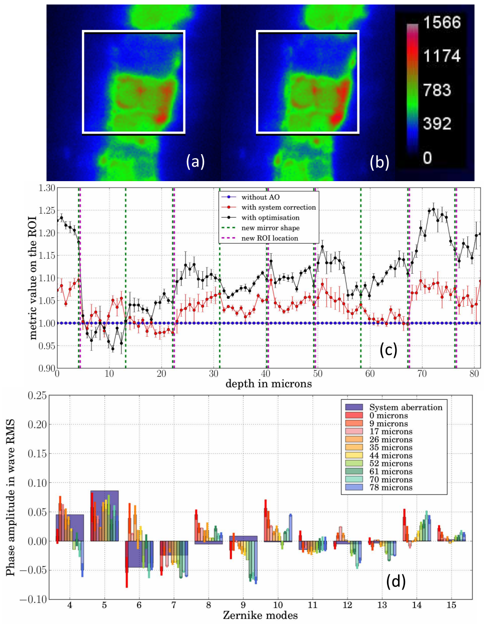

Fig. 6. Results showing the improvements taken when using a refractive index matching FEP mounting tube, again. The images show again part of the pectoral fin. (a,b) are images taken for a flat mirror shape and for a mirror shape optimized directly on the fish respectively. As discussed in the text - the improvements here are marginally (although clearer in the original data than that shown here). The white square corresponds to the ROI on which the optimization is performed and is 19 μm wide. (c) gives the metrics normalized to the uncorrected metric (blue) for the case of system only correction (red) and full sample correction (black) . The green vertical lines correspond to where the mirror has been optimized. The purple vertical line shows when the ROI has been moved. (e) represents the Zernike mode amplitude at different depths.

centered on a portion of the image that contained fine structure. A second z–stack with finer axial resolution was then recorded over the same depth range using 100 axial positions giving Nyquist sampling in the axial direction. The mirror shape was changed based upon the results of the previous low sampling stack - using the closest optimized image. For each of the 100 points along the stack, in addition to the optimized image (Fig. 5(c)), two additional images were recorded using a flat mirror shape (Fig. 5(a)), and with system–only aberration correction (Fig. 5(b)) (where "system" refers to the optics and the mounting pipette), corresponding to a mirror shape optimized using beads when positioned at a depth of 200 μm from the first surface of the cylinder. Figure 5(d) shows the corresponding three metric values, normalized to the incorrect case. On average over the stack, the metric improves by 380% from the AO off image (blue) to the AO on image (black). Figure 5(e) gives the amplitude of the first 12 Zernike modes (Piston, Tip and Tilt excluded) generated on the mirror during the z–stack. Clearly the aberrations do change as a function of depth - but they are also clearly dominated by system aberrations. The exposure time was between 13 ms and 27 ms per frame depending on the brightness of the feature and to perform an optimisation of 12 modes, with 3 images per modes took about 15 seconds. Our system was not, however, optimized for speed, and this will be improved when we move to imaging live-fish.

#164711 - $15.00 USD Received 14 Mar 2012; revised 14 May 2012; accepted 15 May 2012; published 29 May 2012

FEP (fluorinated ethylene propylene) polymer tubing that is refractive index–matched to the water can be used [24] to minimize aberrations. However, refractive index inhomogeneities in the tube and, in the case of deep imaging, sample induced aberrations still contribute to the image quality and contrast degradation. As with the glass pipette, a calibration was made by optimizing using a bead positioned at the centre of the tube (Adtech Polymer Engineering FI 1.3x1.6).

Once complete the zebrafish was placed in the polymer tube filled with water and the same procedure followed as with the glass tube. First a calibration stack over 80 μm composed of ten optimized sections was performed and the mirror shape recorded for each depth. Subsequently, another stack composed of 100 images was recorded using the optimized mirror shape for a given depth determined from the previous calibration, as before. Figures 6(a) and 6(b) shows images with respectively with the AO off and on. The optimized image presents brighter features. In Fig. 6(c), the metric values for the uncorrected, system-only correction, and full correction are shown. The vertical green and purple dashed lines show respectively when the mirror shape has changed, and when the ROI has been displaced. The optimization leads to higher metric values, except in the range [4-12 μm] where a saturated localized spot has confused the metric value. The error bars represent the standard deviation on the metric value calculated for four images taken at each depth and normalized by the uncorrected case. The error bars are 0.026 on average. The average improvement in metric value is $10\% \pm 2.6\%$ over the whole stack. The Zernike mode amplitudes are given in Fig. 6(d) for each depth. The contribution of each mode remains small, as compared, for example, with the Maréchal criteria $\lambda/14$ RMS), which indicates that the wavefront distortion is low. The error on the Lorentzian fits, is, on average 0.013 waves RMS.

We calculated the Raleigh range of the illumination beam to be around 7 μm which would give a “field of view”' (defined here as an area over which the illumination beam is at its minimum thickness) of around 14 μm. This is clearly smaller than the field of view shown in the results presented in Figs. 5 and 6 and is one of the reasons for the fall off in image quality way from the centre. In general, the degradation of the imaging performance away from the central point is of great interest in AO - and is also an area which is relatively unexplored in microscopy. The lateral resolution of the system (in the centre of the field of view) is diffraction limited at 1 μm (given by $2.44\lambda/(2\text{N.A.})$). The axial resolution is harder to measure. In theory, it is governed by the thickness of the illumination sheet which is around 2 μm assuming there is no broadening of the illumination beam. In practice, when observing the beads we could make an upper bound estimate based on the fact that when we viewed one bead we did not see light contamination from neighbouring beads in the axial direction. The spacing of the beads was typically 8 μm and so we can say the axial resolution is between 2 and 8 μm.

5. Discussion

We have demonstrated that the correction of aberrations using AO on the emission path of a SPIM microscope enables sharper and more contrasted images. As well as correcting aberrations on the emission path the AO also corrects for beam displacements on the illumination path. Modal wavefront sensorless AO was found to be a particularly useful optimization technique which was less sensitive to small motions in the sample compared to other optimization techniques. Issues which required careful attention included the following:

- a careful choice of the image metric was required to avoid convergence problems.
- the waist of the light sheet has to be well centered in the ROI, otherwise the out of focus part of the specimen is illuminated and contributes to the sharpness reduction and this can clearly not be corrected by the AO system in the imaging arm.

#164711 - $15.00 USD Received 14 Mar 2012; revised 14 May 2012; accepted 15 May 2012; published 29 May 2012

- as with all microscope AO systems, when scattering occurs on both the excitation and/or the emission path, the resultant blurring and increase in background signal degrades the signal-to-noise ratio and reduces the effectiveness of the metric.

In Fig. 5 we have clearly demonstrated the successful application of AO to SPIM, however the results shown in Fig. 6 show that the aberrations in the sample itself were rather small and in this particular case most of the image improvement could be obtained by the proper choice of mounting pipette. Clearly this leads to the conclusion that AO is not actually required - but this is only for this one particular sample arrangement. We have noticed that the significant aberrations do occur in some samples, especially at depth. The main point here is that we have successfully demonstrated AO in SPIM, and also shown how it is a useful way of characterizing the aberrations as a function of depth. In a future paper we aim to show the combination of AO, as described in this paper, with our heart sycnhronization system [18] in order to demonstrate AO corrected images within the living heart. Further improvements may be possible with the addition of AO on the illumination arm of a SPIM system to maximize the optical sectioning capability throughout the sample and potentially to use point spread function engineering of the light path for improved resolution.

Acknowledgments

The authors wish to acknowledge funding from a Research Excellence award from the British Heart Foundation, and the Engineering and Physical Science Research Council (Grant EP/I010173/1). All samples were used in accordance with UK Home Office rules. Thanks to Prof. John Mullins and his team at Edinburgh University for their help and for supplying the fish.

#164711 - $15.00 USD Received 14 Mar 2012; revised 14 May 2012; accepted 15 May 2012; published 29 May 2012